Three-dimensional meso-scale finite element modeling of bonded joints between a near-surface mounted FRP strip and concrete

J.G. Teng[1,*], S.S. Zhang[1], J.G. Dai[1] and J.F. Chen[2]
[1]Department of Civil and Structural Engineering
The Hong Kong Polytehnci University, Hong Kong, China
[2]Institute for Infrastructure and Environment, School of Engineering,
The University of Edinburgh, Edinburgh, EH9 3JL, Scotland, UK
*cejgteng@polyu.edu.hk

Abstract: This paper presents a three-dimensional (3-D) meso-scale finite element (FE) model for near-surface mounted (NSM) FRP strip-to-concrete bonded joints established using the general-purpose FE software package MSC.MARC. In the FE model, elements of the order of 1 mm in size are employed. The concrete is simulated using the orthogonal fixed smeared crack model while the FRP and the adhesive are treated as linear brittle-cracking materials. The FE model is calibrated and verified using results of well-documented bonded joint tests. Using the verified FE model, the failure process of NSM FRP strip-to-concrete bonded joints is carefully studied; furthermore, the local bond stress distributions and the bond-slip relationships are extracted and analyzed. This 3-D meso-scale FE model offers a powerful tool for deployment in further investigations to establish bond-slip models and bond strength models for NSM FRP strip-to-concrete bonded interfaces. While the present study is focused on NSM FRP strips, the proposed modeling approach is generally applicable to NSM FRP bars of other cross-sectional shapes.

Keywords: three-dimensional (3-D) analysis, meso-scale modeling, finite element (FE) modeling, near surface mounted (NSM) FRP, strip, interface, bond behavior

1 Introduction

Reinforced concrete (RC) members can be strengthened with near-surface mounted (NSM) FRP bars of various cross-sectional shapes [1]. Over recent years, the NSM FRP strengthening method has become an attractive alternative to the popular technique of externally bonded FRP plates/sheets [2]. To develop a reliable design theory for the NSM FRP technique, a fundamental issue to clarify is the bond behavior between NSM FRP and concrete. The conventional approach for studying this bond behavior is to conduct tests on NSM FRP-to-concrete bonded joints (simply referred to as bonded joints for simplicity where appropriate) [3-8]. However, test data of NSM FRP-to-concrete bonded joints are still very limited compared with those available for externally bonded FRP reinforcement.

The behavior of NSM FRP-to-concrete bonded joints is more complicated than that of externally bonded FRP-to-concrete joints as the former depends on many more parameters including the material, shape, surface configuration and size of the NSM FRP bar, the shape and size of the groove, and the properties of both the concrete substrate and the adhesive filler (generally an epoxy). As a result, it is very difficult to achieve a comprehensive understanding of the effects of all these factors on the bond behavior between NSM FRP and concrete through

(exhaustive) laboratory tests only. In addition, it is highly challenging if not impossible to accurately capture the local details of bond behavior between NSM FRP and concrete in a laboratory test (e.g. the local bond-slip response) due to difficulties in placing strain gages on the NSM FRP bar without disturbing the bond properties; this is in contrast to externally bonded FRP plates/sheets where strain gages can be attached to their surface to monitor the local bond behavior. Given the above considerations, reliable finite element (FE) studies are very attractive to supplement experimental studies in understanding the bond behavior between NSM FRP and concrete.
A review of the existing literature indicates that an accurate FE model for NSM FRP-to-concrete bonded joints, with sufficient details in terms of constitutive laws for the constituent materials, is not yet available. Lundqvist et al. [9] used the damaged plasticity model for concrete to study the anchorage length of NSM FRP strips in beam pull-out tests but did not succeed in predicting the failure loads of the tests because the analysis stopped prematurely due to numerical problems. Lundqvist et al. [10] examined only the linear elastic behavior of NSM FRP-to-concrete bonded joints. In other existing studies [e.g. 3, 11], interface elements with an assumed bond-slip relationship were used to simulate the behavior of NSM FRP-to-concrete bonded joints; these FE models are not truly predictive as their predictions depend on the bond-slip relationship adopted for the FE model.

In contrast to the lack of FE studies on NSM FRP-to-concrete bonded joints, extensive research has been undertaken on externally bonded FRP-to-concrete bonded joints [e.g. 12-14]. This work has shown convincingly that a reliable FE model employing elements of very small sizes (referred to as meso-scale elements) can be a powerful and economical alternative to laboratory testing to gain a full understanding of the complex behavior of FRP-to-concrete bonded joints and to generate numerical results for the development of a local bond-slip relationship model. Lu et al. [12] developed the first reliable 2-D meso-scale FE model using elements of the order of 0.5 mm and an orthogonal fixed smeared crack model to simulate the local bond-slip behavior and local failure process of externally bonded FRP-to-concrete bonded joints. Adopting a similar approach, this paper presents a 3-D meso-scale FE model for NSM FRP-to-concrete bonded joints. The present paper is focused on the FE modeling of bonded joints between NSM FRP strips (i.e. bars of narrow rectangular section) and concrete for the simulation of failure process and the prediction of the local bond-slip relationship, although the proposed modeling techniques can also be employed to model the bond behavior of NSM FRP bars of other cross-sectional shapes.

2 Bond tests and FE modeling

2.1 Bond test methods

Two popular bond test methods have been adopted by researchers to investigate the bond behavior of FRP bars near-surface mounted to concrete: (1) the beam pull-out test, and (2) the direct pull-out test. The beam pull-out test for NSM FRP bars was derived from the pull-out bending test for assessing the bond characteristics of conventional steel bars and was used to study the bond behavior of NSM FRP bars by Nanni et al. [15]. The direct pull-out test is conducted on a concrete block embedded with an NSM FRP bar and is usually conducted under displacement control. The direct pull-out test setup has three main variations: traditional one-side direct pull-out test [e.g. 4, 6], two-side direct pull-out test [e.g. 16], and C-shaped block direct pull-out test [e.g. 3]. In the present study, the NSM CFRP strip-to-concrete bonded joint specimens analyzed are from Li et al. [6], in which the one-side direct pull-out test

approach (Fig. 1) was adopted. These specimens were selected for analysis because all needed details of the tests including the measured strain distributions of the FRP strip are readily available to the authors.

2.2 Li et al.'s pull-out tests

A total of five NSM CFRP strip-to-concrete bonded joints were tested by Li et al. [6], with the bond lengths being 30 mm, 100 mm, 150 mm, 200 mm and 250 mm respectively. The concrete block had a square section of 150 mm$\times$150 mm and a length of 350 mm, and the bonded region of the NSM strip started at 50 mm away from the loaded end (Fig. 1). The groove size had a design width w_g of 8 mm and a design height h_g of 22 mm, but post-preparation measurements indicated that the actual values were about 9 mm and 22 mm.

The concrete had an averaged cube compressive strength f_{cu} of 29 MPa. The cylinder compressive strength f_c can be estimated from

$$f_c = 0.8 f_{cu} \tag{1}$$

and the tensile strength f_t can be estimated as [17]

$$f_t = 1.4\left(\frac{f_c - 8}{10}\right)^{\frac{2}{3}} \tag{2}$$

The groove-filling material was a two-component epoxy adhesive with a mixing ratio of 2 (resin):1 (hardener) by weight. The tensile strength and elastic modulus of the adhesive averaged from five tensile coupon tests were 42.6 MPa and 2.62 GPa respectively. The Poisson's ratio of the epoxy is assumed to be a typical value of 0.35. The CFRP strips had a thickness of 2 mm and a width of 16 mm. The ultimate tensile strength and elastic modulus of the CFRP strips were 2068 MPa (according to the manufacturer) and 151 GPa (deduced from readings of strain gauges installed on the exposed part of the NSM CFRP strip in the bonded joint tests), respectively. Two CFRP strips were bonded together using the groove filling adhesive, forming a compound strip whose total thickness was approximately 5 mm (i.e., 4 mm of CFRP plus about 1 mm of adhesive), whereas the width was still 16 mm. The use of a compound strip instead of a normal strip is to allow the installation of strain gauges between the two strips of a compound strip so that the strain gauges would not interfere with the interfacial behavior. It should be noted that the elastic modulus of the compound strip for FE modeling in this study was modified according to its real thickness as follows: $E_f = 151\times 4/5 = 120.8\ MPa$. The Poisson's ratio of the CFRP compound strip was assumed to be 0.2. The effect of using a nearly zero Poisson's ratio (0.002) was also explored before choosing this Poisson's ratio for use in the parametric study; it was found that such a small Poisson's ratio led to load-displacement curves which are almost identical to those obtained with a Poisson's ratio of 0.2 with the ultimate loads differing by less than 1%. Details of the specimen are listed in Table 1.

2.3 Finite element model for bonded joint specimens

The FE model was built using the general-purpose FE software package MSC.MARC [18] with the tension-softening curves and the shear retention factor models for the cracked concrete incorporated through user-defined subroutines. Based on the configuration of the test setup, only half of the specimen was modeled by taking advantage of symmetry; that is, the horizontal

displacements on the plane of symmetry (Fig. 2) were prevented. Furthermore, the 50 mm high bottom layer of concrete was not taken into account to reduce significantly the computational time; this simplification should only have an insignificant effect on the crack propagation near the NSM bar as was found through some preliminary FE analyses. The bottom surface of the numerical model was restrained against vertical displacements but was allowed to move horizontally (Fig. 2). The horizontal restraints at the loaded end of the concrete block and the vertical restraints at the far end of the concrete block (Fig. 1) were simulated by setting the corresponding displacements to zero in the FE model. The numerical specimen was loaded by imposing a displacement at the end of the CFRP strip.

The 3-D, eight-node, first-order, isoparametric solid element with full Gaussian integration available in MSC.MARC was used to model the concrete block, the CFRP strip and the adhesive. The FE mesh in and near the bonded region was finer than elsewhere. After a convergence study to be presented later, the final mesh of the FE model was determined as follows: 1) the element size for the FRP strip was 0.83 mm in its thickness direction (3 elements), 1.23 mm in its height direction (13 elements), and 1.25 mm in the longitudinal direction; 2) the element size for the adhesive was about 0.5 mm in its thickness direction (4 elements), 1.23 mm in the height direction (13 elements in the strip height region), and 1.25 mm in the longitudinal direction; and 3) the element size for the concrete was 1.25 mm within the central zone of 30 mm from the plane of symmetry, 60 mm from the top surface of the concrete block, and the bonded region plus 10 mm in each direction in the longitudinal direction. The maximum side length of concrete elements in the remaining parts was 2.5mm. The mesh adopted for specimen CS-150 is shown in Fig. 3, which includes an overall view of the mesh and a detailed view near the loaded end.

3 Constitutive laws and material properties

3.1 General

Failure of a NSM FRP-to-concrete bonded joint may occur in one of the three constituent materials (FRP, adhesive and concrete) or at one of the two bi-material physical interfaces (FRP/adhesive and concrete/adhesive interfaces). The former is commonly referred to as cohesion failure while the latter is commonly referred to adhesion failure. Adhesion failure can be and should be avoided through the proper surface preparation of the two adherends so that failure of the bonded joint is determined by the material strengths of the three constituent materials. In theory, cohesion failure can occur in any of the three constituent materials, but existing tests on NSM FRP-to-concrete bonded joints have indicated that in most cases, cohesion failure occurs in the concrete as the adhesive normally has a much high tensile strength than the concrete. In practical applications, it should also be ensured that failure is governed by cohesion failure in concrete through appropriate surface preparation and through the use of an appropriate adhesive as otherwise the strength of concrete cannot be fully utilized. Cohesion failure in FRP is the least likely and is not considered in the present study, but the possibility of cohesion failure in the adhesive is considered in the present study.

Consequently, the modeling of concrete is of particular importance. As mentioned earlier, the so-called meso-scale FE approach was first proposed for externally bonded FRP-to-concrete bonded joints to investigate the interfacial debonding failure process and the local bond-slip relationship by Lu et al. [12]. It should be noted that the meso-scale FE analysis here is different from the meso-mechanical model in which the concrete is treated as a three-phase

composite including the cement matrix, aggregate and matrix-aggregate interface [e.g. 19, 20]. Instead, a meso-scale FE model still treats the concrete as a homogenous material and thus reflects the average response of concrete, but uses very small elements to capture the complex process of cracking of the concrete.

3.2 Modeling of concrete

3.2.1 Modeling approaches for cracked concrete

In the present study, the cracking of concrete was simulated using the orthogonal fixed smeared crack model available in the general-purpose software package MSC.MARC [18], and a very fine FE mesh, which simulates cracking by changing the constitutive relationship, in contrast to the discrete crack concrete model which treats a crack as a geometry entity [e.g. 21]. It allows one crack at one integration point for one-dimensional elements, two orthogonal cracks for two-dimensional elements and three orthogonal cracks for three-dimensional elements.

Besides the orthogonal fixed smeared crack model, two other popular approaches for modeling cracked concrete are the multi-directional smeared crack model and the rotating smeared crack model [22]. In the multi-directional smeared crack model, when the angle between the maximum principal tensile stress and the existing crack direction exceeds a certain value (referred to as the threshold angle hereafter), new cracking occurs perpendicular to the direction of the current maximum principal stress. The rotating smeared crack model can be divided into two main types [22]. The first type is called the non-coaxial rotating smeared crack model, in which the directions of the principal stresses can be different from those of the principal stains; the second type is called the coaxial rotating smeared crack model, in which the directional alignment between the principal stresses and the principal strains is forced. The concept of the rotating smeared crack model has been criticized in that the rotation of the crack lacks physical meaning and some parameters need to be determined empirically [12]. The multi-directional smeared crack model is thought to be the most advanced in theory, but the threshold angle for the appearance of new cracking is difficult to define, and numerical convergence is usually a great challenge. Due to the above considerations, the multi-directional model and the rotating smeared crack model have seldom been incorporated into general-purpose software packages which are capable of handling complicated 3-D nonlinear analysis as well as heavy computation. On the contrary, these software packages usually include the orthogonal fixed smeared crack model. If a good shear retention factor model is employed and the element size is made small enough, accurate FE modeling of crack appearance and propagation is possible using the orthogonal fixed smeared crack model. Indeed, this meso-scale FE method based on the orthogonal fixed smeared crack model has been successfully used by the authors' group in the FE modeling of externally bonded FRP-to-concrete joints [12], and was thus also adopted in the present study.

The smeared crack model for concrete was first introduced by Rashid [23] and since then has been adopted by numerous researchers. One of the intrinsic properties of concrete is its tension-softening behavior (i.e. the stress-strain curve exhibits a descending branch after cracking), which leads to the well-known mesh sensitivity issue. To mitigate the mesh sensitivity problem, Bazant and Oh [24] proposed the crack band model, which relates the element size to the tension-softening behavior of concrete based on the fracture energy concept. The crack band model was adopted in the present study.

3.2.2 Yield and failure surfaces

The yield surface proposed by Buyukozturk [25] (Eq. 3) with the associated flow rule was adopted in this study. The failure surface adopted is a combination of Buyukozturk's [25] model (Eq. 3) and the maximum tensile stress criterion (Eq. 4). The yield surface and the failure surface employed in this study are the criteria recommended by MSC.MARC [18] for modeling concrete.

$$3J_2 + \sqrt{3}\chi\sigma^* I_1 + \xi I_1^{\,2} = (\sigma^*)^2 \tag{3}$$

$$f(I_1, J_2, \theta) = 2\sqrt{3}\sqrt{J_2}\cos\theta + I_1 - 3f_t = 0 \tag{4}$$

where I_1 and J_2 are the first invariant of stresses and the second invariant of deviatoric stresses respectively; ξ, χ and σ^* are material constants and equal to 0.2, $\sqrt{3}$ and $\sigma^{\wedge}/3$ respectively [25]; $\sigma^{\wedge}$ is the yield stress of concrete, taken to be $\frac{f_c}{3}$ in the present study according to Buyukozturk [25] when Eq. 3 is used to define the yield surface and the compressive strength f_c when Eq. 3 is used to define failure surface; f_t is the tensile strength of concrete; and θ is the angle of similarity.

This approach is similar to that used by Chen [26], in which the Mohr-Coulomb criterion and the maximum tensile stress or strain criterion were combined to simulate the behavior of concrete.

3.2.3 Uniaxial compressive stress-strain curve

The following uniaxial compressive stress-strain curve which was modified by Elwi and Murray [27] from Saenz's curve [28] was adopted in this study (Fig. 4):

$$\sigma_c = \frac{E_0\varepsilon}{1 + (R + \frac{E_0}{E_s} - 2)(\frac{\varepsilon}{\varepsilon_0}) - (2R-1)(\frac{\varepsilon}{\varepsilon_0})^2 + R(\frac{\varepsilon}{\varepsilon_0})^3} \tag{5}$$

in which

$$R = \frac{E_0/E_s(\sigma_0/\sigma_u - 1)}{(\varepsilon_u/\varepsilon_0 - 1)^2} - \frac{1}{(\varepsilon_u/\varepsilon_0)} \tag{6}$$

where σ_0 and ε_0 are the maximum stress and the corresponding strain respectively, and are assumed to be the compressive cylinder concrete strength (f_c) and 0.002 respectively following Chen [26]; ε_u and σ_u are the ultimate strain and the corresponding stress respectively, and are assumed to be 0.0038 and $0.85\,f_c$ following Hognestad [29] respectively; If the compressive strain in the concrete reaches 0.0038, the concrete fails by crushing and the stress drops to zero; E_0 is the initial elastic modulus and is calculated according to ACI-318 [30]: $E_0 = 4730\sqrt{f_c}$; and E_s is the secant modulus at the maximum stress: $E_s = \sigma_0/\varepsilon_0$.

3.2.4 Tension-softening curve

Three tension-softening curves were considered in this study: (a) the linear softening curve [31], (b) the bilinear softening curve [32] and (c) the exponential softening curve [33]. The

linear softening curve is based on the assumption that the tensile stress reduces linearly to zero at a crack opening displacement of w_0 (Fig. 5a); the bilinear softening curve is based on the assumption that the tensile stress reduces linearly to 1/3 of the ultimate tensile stress at a crack opening displacement of 2/9 w_0 firstly and then reduces linearly to zero at w_0 (Fig. 5b); and the exponential softening curve is based on the assumption that the softening branch follows the following exponential function [33] (Fig. 5c):

$$\frac{\sigma_t}{f_t} = \left[1 + \left(3.0\frac{w}{w_0}\right)^3\right] e^{\left(-6.93\frac{w}{w_0}\right)} - 10\frac{w}{w_0}e^{(-6.93)} \qquad (7)$$

where w is the crack width (i.e. crack opening displacement), and w_0 is the crack width at the complete release of stress or fracture energy. The w_0 value for these three tension-softening models is different. It can be related to the tensile fracture energy G_{ft} as $w_0 = 2G_{ft} / f_t$ for the linear softening curve, $w_0 = 3.6G_{ft} / f_t$ for the bilinear softening curve and $w_0 = 5.4G_{ft} / f_t$ for the exponential softening curve respectively, based on the following relationship:

$$\int \sigma_t dw = G_{ft} \qquad (8)$$

The tensile strength of concrete f_t (Eq. 2) and the tensile fracture energy G_{ft} (Eq. 9) proposed by CEB-FIP [17] were used in this study.

$$G_{ft} = (0.0469D_a^2 - 0.5D_a + 26)(\frac{f_c}{10})^{0.7} \qquad (9)$$

where D_a is the maximum aggregate size.

The unloading and reloading curves of the tensile stress-crack opening displacement relationship follow the linear path that passes through the origin of the coordinate system as shown in Fig. 5.

3.2.5 Shear retention factor

The shear retention factor is the ratio of secant shear modulus of concrete after cracking to that before cracking, which reflects the shear stress-strain (or slip) relationship after cracking of concrete and significantly influences the predicted behavior of cracked concrete. In the present FE model, the shear stress-slip relationship is preferred to the shear stress-strain relationship, considering that the later one is mesh sensitive. Six popular shear stress-slip models were examined. Typical shear stress-slip curves of these six models are shown in Fig. 6 for a crack width of 0.5 mm. The secant shear moduli G_{cr} for the six models are given in Eqs. 10 to 15 below.

1) Bazant and Gambarova's shear stress-slip model [34]

$$G_{cr} = \frac{\tau_u}{\varepsilon_{nt}^{cr}} \frac{2.45/(0.245f_c) + 2.44[1 - 4/(0.245f_c)]\psi^3}{1 + 2.44[1 - 4/(0.245f_c)]\psi^4} \qquad (10)$$

where $\tau_u = 0.245 f_c \frac{0.01D_a^2}{0.01D_a^2 + w^2}$ is the maximum shear stress, D_a is the maximum aggregate size, $\psi = \frac{\Delta}{w}$ is the ratio of the crack slip $\Delta = b_{cr}\varepsilon_{nt}^{cr}$ to the crack width $w = b_{cr}\varepsilon_{nn}^{cr}$ where b_{cr} is the crack band width, and ε_{nt}^{cr} and ε_{nn}^{cr} are the shear strain and normal strain of the crack

respectively.

2) Walraven and Reinhardt's shear stress-slip model [35]

$$G_{cr} = -\frac{f_{cu}}{30\varepsilon_{nt}^{cr}} + [1.8w^{-0.8} + (0.234w^{-0.707} - 0.2) f_{cu}]b_{cr} \geq 0 \qquad (11)$$

3) Yamada and Aoyagi's shear stress-slip model [36]

$$G_{cr} = \frac{3.5}{w} \qquad (12)$$

4) Okamura and Maekawa's shear stress-slip model [37]

$$G_{cr} = \frac{b_{cr}^2 \varepsilon_{nt}^{cr}}{w^2 + \Delta^2} 3.8 f_c^{1/3} \qquad (13)$$

5) Kang's shear stress-slip model [38]

$$G_{cr} = (0.543w^{-0.585} + 0.199)\sqrt{f_c}(b_{cr})^{0.72}(\varepsilon_{nt}^{cr})^{-0.28} \qquad (14)$$

6) Vecchio and Lai's shear stress-slip model [39]

$$G_{cr} = \frac{b_{cr}^2 \varepsilon_{nt}^{cr}}{\delta^2 + \Delta^2} \frac{\sqrt{f_c}}{0.31 + \frac{24w}{D_a + 16}} \qquad (15)$$

where $\delta = \dfrac{0.5\sqrt{f_c} \Big/ (0.31 + \frac{24w}{D_a + 16}) + f_{cu}/30}{1.8w^{-0.8} + (0.234w^{-0.707} - 0.2) f_{cu}}$.

Once the scant shear modulus G_{cr} of the cracked concrete is determined, the shear retention factor β_s of the concrete after cracking can be calculated as [40]

$$\beta_s = \frac{G_{cr}}{G_0 + G_{cr}} \qquad (16)$$

where G_0 is the shear modulus of un-cracked concrete.

3.3 Modeling of FRP and adhesive

The compound CFRP strip was modeled as an elastic isotropic brittle material with its stress-strain curve shown in Fig. 7a. Although the compound CFRP is an orthotropic material in reality [41], the isotropic assumption here should not lead any significant errors given that the Poisson's ratio has little effect on the predictions as mentioned early and the FRP strip is very thin (so that little deformation in the specimen is due to the lateral deformation of the strip).

The adhesive was also modeled as a linear elastic isotropic brittle material in tension (Fig. 7b), and its cracking behavior was simulated using the same approach as that for concrete. For compression-dominated behavior, the adhesive was modeled as an elastic perfectly-plastic material obeying the von Mises yield criterion. For tension-dominated behavior, the maximum tensile stress criterion was still adopted to determine the initiation of cracking. The shear retention factor was set to be zero (A very small value of 0.002 was actually used to avoid

numerical problems) after cracking based on the consideration that the aggregate interlocking effect does not exist in an adhesive.

4 Calibration of the FE model

In this section, FE predictions of specimen CS-150 tested by Li et al. [6] are examined to calibrate the proposed FE model. Mesh convergence, the tension-softening model and the shear retention factor model for concrete are discussed below.

4.1 Mesh convergence

Chen and Pan [42] and Lundqvist et al. [10] conducted 3-D linear elastic FE analyses to study stress concentration in respectively external FRP-to-concrete and NSM FRP-to-concrete bonded joints. Teng et al. [43] conducted 2-D linear elastic FE analyses to study stress concentration near plate ends in RC beams strengthened with an externally bonded plate. In their FE models, very small elements were used (e.g. the smallest elements used near the plate ends were 0.1 mm in size). Although stress singularity points also exist in the present problem in the elastic range, it is not necessary to employ very small elements as in these two previous studies for two reasons: first, this study is more concerned with the failure process rather than the precise elastic stress distributions near stress singularity locations; second, once cracking occurs, stress concentration at stress singularity points is released or much reduced.

The mesh convergence study considered three different meshes composed of cube or nearly cubic elements. The crack band width (characteristic length) used in the present study was the cubic root of the volume of the element (i.e. the element side length if the element is cubic). In transforming a stress-strain relationship to a stress-crack width relationship, this crack band width (characteristic length) was used. These meshes include:

1) Mesh 1: In this mesh, most concrete elements have a size of 5 mm near the groove and a maximum size of 7.5 mm away from it. The adhesive is modeled using one element in the thickness direction. The CFRP is modeled using one and three elements respectively in the thickness and height directions.
2) Mesh 2: In this mesh, most concrete elements have a size of 2.5 mm near the groove and a maximum size of 5 mm away from it. The adhesive is modeled using two elements in the thickness direction. The CFRP strip is modeled using 2 and 6 elements in the thickness and height direction respectively; and
3) Mesh 3: In this mesh, most concrete elements have a size of 1.25 mm near the groove and a maximum size of 2.5 mm away from it. The adhesive is modeled using 4 elements in the thickness direction. The CFRP strip is modeled using 3 and 13 elements in the thickness and height directions respectively.

The shear retention factor deduced from Okamura and Maekawa's shear stress-slip model [37] and the exponential tension-softening curve were adopted in the mesh convergence study. The load-displacement curves obtained from the three meshes are shown in Fig. 8. Mesh 3 (with the smallest concrete element size being 1.25mm) produced similar results to Mesh 2 (with the smallest concrete element size being 2.5mm), but Mesh 1 led to a relatively large error of the predicted ultimate load compared with the other two meshes. Mesh 3 was treated as a converged mesh and adopted in the subsequent FE analyses.

4.2 Tension-softening curve

As mentioned earlier, three tension-softening models were studied to investigate whether they influence the FE predictions when the same fracture energy is adopted in the crack band model. The load-displacement curves obtained using the three tension-softening models are shown in Fig. 9. These results show that: (a) within the linear range, the three models lead to almost the same results; (b) in the nonlinear range between about 27 kN and the peak load, some differences exist between the results from the three tension-softening models; the linear one leads to the largest load while the exponential one leads to the smallest load. The differences between the ultimate loads, however, are very small; and (c) in the descending range, predictions obtained with the three tension-softening models are also slightly different. On the whole, these three tension-softening models lead to very similar predictions for the overall behavior of the test specimen. As a result, the exponential curve was employed in the subsequent FE analyses.

4.3 Shear retention factor

Having chosen the appropriate mesh and the tension-softening model, the next important step was to examine the shear retention factor models. The load-displacement curves from the test was not directly given by Li et al. [6], but the strain distributions in the CFRP strip of specimen CS-150 were provided. The displacement at the loaded end was calculated by integrating the axial strains in the FRP from the free end to the loaded end with the slip at the free end assumed to be zero. Accordingly, for comparison purpose, the displacement used for plotting the load-displacement curve obtained from the FE analysis was calculated by subtracting the displacement at the loaded end by that at the free end.

The FE load-displacement curves for the six shear retention factor models are compared in Fig. 10 with that from the integration of strains in the FRP strip from the test. The predicted ultimate loads and the corresponding displacements are listed in Table 2. As can be seen from Fig. 10, all the curves from the FE model have slightly larger slopes than that from the test. This is probably because there were too few strain measurement points on the FRP strip so the integration of strains using the trapezoidal rule overestimates the displacement. By examining the load-displacement curves, it can be found that Bazant and Gambarova's model [34] leads to a load-displacement curve similar to the test in shape but overestimates the ultimate load and the corresponding displacement. The load-displacement curve predicted with Walraven and Reinhardt's model [35] deviates significantly from the test curve in shape; large errors are seen for the ultimate load and the corresponding displacement. Yamada and Aoyagi's model [36] and Vecchio and Lai's model [39] lead to load-displacement curves similar in shape to the test curve but both substantially underestimate the ultimate load. Kang's model [38] leads to acceptable results and performs better than all the above models, with the ultimate load and the corresponding displacement being underestimated. Okamura and Maekawa's model [37] leads to the closest predictions of the test results among the six models examined here, although it also slightly overestimates the ultimate load and corresponding displacement. Based on these comparisons, the model by Okamura and Maekawa [37] was employed in the subsequent FE analyses.

5 Additional comparisons and failure mechanics

In this section, FE predictions of the ultimate loads of the five specimens tested by Li et al. [6] are compared with the test results. Results for Specimen CS-150 are examined in detail to understand the failure process, the strain distribution in FRP and local bond-slip relationship.

5.1 Ultimate loads

The ultimate loads are compared with the test results for all the five specimens in Fig. 11 and Table 3. Clearly, the FE predictions are in excellent agreement with the test results, with the average, standard deviation (STD) and coefficient of variation (CoV) of the FE-to-test ultimate load ratios being 1.042, 0.100 and 0.096 respectively. This comparison further demonstrates the accuracy of the proposed FE model in predicting the test ultimate loads.

5.2 Failure mechanism and process

A careful examination of the cracking strain (i.e. *the total strain minus the elastic tensile strain)* distribution from the FE model revealed that there was little if any cracking in the adhesive in the bonded joint. This is mainly because: (a) the adhesive has a much higher tensile strength than the concrete (about 23 times) and a smaller elastic modulus (about one tenth), so under the same deformation, concrete cracking occurs first; and (b) the surface of the CFRP strip is taken as a smooth surface, leading to smaller lateral forces than can be expected from a ribbed FRP bar. As a result, the failure process of the bonded joint can be expected to depend strongly on the initialization and propagation of cracking in the concrete.

The deformation and cracking behavior of concrete in an NSM FRP bonded joint as predicted by the meso-scale FE model is illustrated in Fig. 12, in which the values of the maximum principal cracking strain in the global coordinate system in the concrete are shown. Before cracking, the stress state in the concrete and that in the adhesive are dominated by shear stresses with very small tensile normal stresses (Fig. 12b). The dashed lines in Fig. 12b show the idealized deformation patterns in the concrete and the adhesive. As the applied load increases, the shear stress and the maximum principal stress (at approximately 45 degrees to the load direction) in the concrete also increase. When this principal tensile stress reaches the tensile strength of concrete, micro-cracking occurs with the direction of micro-cracking being perpendicular to the maximum principal stress. A possible crack pattern is shown in Fig. 12c. Between the concrete cracks, fish-spine-like columns form. The normal stress on the groove lateral edges is compressive as a result of the restraint from the outer concrete. On the crack surfaces, the behavior is governed by tension-softening and aggregate shear locking. Fig. 12a shows the cracking strain distribution on the top surface in a segment of the bonded joint from FE analysis.

Fig. 13 shows the distributions of cracks (represented by values of the maximum principal cracking strain) in the concrete at different load levels as marked on the load-displacement curves in Fig. 10; these distributions demonstrate the initiation and propagation of cracks. When the load is only 6.5% of the ultimate load (Point A in Fig. 10), most of the concrete is in the elastic range except for only a very small region near the loaded end where a few micro-cracks exist. When the load increases to 20% (Point B in Fig. 10), large cracking strains are experienced near the loaded end and the cracking region becomes larger. The cracking

region grows continuously with increases of the applied load (Points C and D in Fig. 10). As the load continues to increase to higher levels (Points E and F in Fig. 10), the cracking region continues to propagate along the bondline. Apparent cracks on the top surface at an angle of about 45 degrees to the axis of the CFRP strip are observed. As the applied load increases to 84% of the predicted ultimate load (Points G, H and I in Fig. 10), the cracking region spreads over the whole bond length, and a large transverse crack appears near the free end of the bonded region. At the same time, the inclined cracks mentioned above become more pronounced. Comparing Fig. 13i with Fig. 13j clearly shows that these inclined cracks and the large transverse crack exhibit excellent agreement with those observed in the test.

5.3 Strain distributions in the CFRP strip

The predicted distributions of axial strain at the centroid of the CFRP strip cross-section along the bond length are compared with the test results in Fig. 14 for specimen CS-150. It should be noted that the ultimate load obtained from the FE analysis is slightly larger than that from the test, so the strain distributions from the FE analysis were adjusted for each load level for more reliable comparison, according to the ultimate load ratio between test and FE analysis (i.e. the strain values from the FE analysis at each load level were multiplied by the ultimate load ratio of 0.96). When the load is less than 72% of the ultimate load, the FE strain distributions are in very close agreement with the test results. Small discrepancies exist between the two sets of results when the load level is close to the ultimate load.

5.4 Local bond-slip relationship

Once the strain distributions in the CFRP strip at different load levels are available, the local bond stresses and slips can be calculated using the following central difference approach:

$$\tau_0 = \tau(x_0 = 0) = 0 \tag{17}$$

$$\tau_i = \frac{t_f E_f}{2C_{failure}}\left(\frac{\varepsilon_i - \varepsilon_{i-1}}{x_i - x_{i-1}} + \frac{\varepsilon_{i+1} - \varepsilon_i}{x_{i+1} - x_i}\right), \quad i = 1, ..., n \tag{18}$$

$$\tau_{n+1} = \tau(x_{n+1} = l_b) = \frac{t_f E_f}{C_{failure}} \frac{\varepsilon_{n+1} - \varepsilon_n}{x_{n+1} - x_n} \tag{19}$$

$$s_0 = s(x = 0) = s_{free\,end} \tag{20}$$

$$s_i = s_{i-1} + \frac{1}{2}(\varepsilon_{i-1} + \varepsilon_i)(x_i - x_{i-1}) \quad \text{with} \quad i = 1, ..., n+1 \tag{21}$$

where n is the number of divisions along the bond length of the FRP strip (n is equal to 119 in the FE analysis and 5 in the test); x is the coordinate along the bond length originating from the free end; ε is the axial strain in the FRP strip; τ_0, τ_{n+1} and τ_i are the bond shear stresses at the free end, at the loaded end and at x_i in the bonded region of FRP strip respectively; s_0 s_{n+1} and s_i are the slip values at the free end, at the loaded end and at x_i in the bonded region respectively; h_f, t_f and E_f are the height, thickness and elastic modulus of the FRP strip respectively; and $C_{failure}$ is the perimeter of the failure surface at x_i which was taken to be the perimeter of the groove in the present study.

The local bond stress distributions from the FE analysis and from the test along the bond length at different load levels are shown in Fig. 15 and Fig. 16 respectively. The predicted local bond stress distribution is somewhat different from that deduced from strain measurements because of the limited number of strain gauges in the bonded region. As shown in Fig. 15, the peak bond stress increases with the applied load but its location remains unchanged at about 5 mm from the loaded end in the initial stage of loading. When the load increases to 58.7% of the ultimate load, the peak bond stress reaches about 8 MPa. As the load further increases, the location of the peak bond stress moves progressively towards the free end. At the same time, the value of the peak bond stress increases slightly further and reaches a stable value of about 9 MPa. The maximum local bond stress obtained from the FE analysis is about 9 MPa, larger than that from the test which is about 7 MPa. This is reasonable because the latter is an average bond stress in a region between two strain gages and only seven strain gauges were installed along the FRP strip, while the former is a local value. The large fluctuations in the FE bond stress distribution observed for externally bonded FRP-to-concrete joints [12] do not appear in the present results for an NSM FRP-to-concrete bonded joint, indicating that the effect of concrete cracking on the bond stress distribution on the surface of the FRP strip is largely eliminated by the adhesive layer which experiences nearly no cracking.

Fig. 17 shows the FE predicted local bond-slip curves at 2.5 mm, 5 mm, 10 mm, 15 mm, 20 mm, 30 mm, and 40 mm from the loaded end. The local bond-slip relationship becomes stable at and beyond about 20 mm from the loaded end. Of the deduced bond-slip curves for different locations along the bond length, the one nearest the loaded end has the smallest peak bond stress value; the value of the peak bond stress increases with the distance from the loaded end. This is because a short distance from the loaded end is necessary for the confining pressure from the surrounding concrete and the adhesive to the FRP strip to develop fully. This observation also indicates that a reasonably long bond length is needed in a pull-out test to obtain a reliable local bond stress-slip relationship for NSM FRP strips.

6 Conclusions

This paper has presented a 3-D meso-scale FE model for near-surface mounted (NSM) FRP-to-concrete bonded joints. The FE model employed elements whose size is of the order of 1 mm to capture the complex fracturing process of concrete and was implemented using the general-purpose FE program MSC.MARC. Based on the results presented in this paper, the following conclusions can be drawn:

1) When the crack band model based on the fracture energy concept is employed, the mesh sensitivity issue is avoided.
2) The shear retention factor representing the aggregate interlocking effect of concrete has a significant effect on the predicted behavior of NSM FRP-to-concrete bonded joints. Six shear retention factor models were assessed in this study. Okamura and Maekawa's model [37] was found to lead to accurate results and was adopted in the proposed FE model.
3) In the present study, the FE model predicted no cracks in the adhesive; this is because the adhesive had a much higher tensile strength and a much lower elastic modulus than the concrete. This result is in agreement with the experimental observation that in most tests, failure occurred in the concrete provided the adherend surfaces were appropriately prepared and the adhesive was sufficiently strong.
4) The load-displacement curves and the strain distributions in the NSM FRP strip from FE analysis are in close agreement with the test results. The FE local bond stress distribution is

significantly different from the test distribution and this discrepancy is due to the limited number of strain gauges installed along the bond length of the FRP strip in the test.

5) The present study has been focused on NSM FRP strips. The proposed modeling approach has the potential for application to NSM FRP bars of other cross-sectional shapes.
6) The proposed FE model provides a powerful and economical alternative to laboratory testing to gain a full understanding of the behavior of NSM FRP-to-concrete bonded joints and to generate numerical results for the development of a bond-slip model.

Acknowledgement

The authors are grateful for the financial support received from the Research Grants Council of the Hong Kong Special Administrative Region (Project No: PolyU 5173/04E) and the National Basic Research Program of China (i.e. the 973 Program) (Project No.: 2012CB026201).

References

[1] De Lorenzis, L., and Teng, J. G. (2007). "Near-surface mounted FRP reinforcement: an emerging technique for strengthening structures." *Composites: Part B*, 38(2), 119-143.

[2] Teng, J. G., Chen, J. F., Smith, S. T., and Lam, L. (2002). *FRP-strengthened RC Structures*, West Sussex: Wiley.

[3] De Lorenzis, L., Lundgren, K. and Rizzo, A. (2004). "Anchorage length of near-surface mounted fiber-reinforced polymer bars for concrete strengthening-Experimental investigation and numerical modeling." *ACI Structural Journal*, 101(2), 269-278.

[4] Blaschko, M. (2003). "Bond behaviour of CFRP strips glued into slits." *Proceedings, 6th International Symposium on Fibre-Reinforced Polymer (FRP) Reinforcement for Concrete Structures*, 8 -10 July 2003, Singapore, pp. 205-214.

[5] Sena Cruz, J. M., and Barros, J. A. O. (2004). "Bond between near-surface mounted carbon-fiber-reinforced polymer laminate strips and concrete." *Journal of Composites for Construction, ASCE*, 8(6), 519-527.

[6] Li, R., Teng, J. G., and Yue, Q. R. (2005). "Experimental study on bond behavior of NSM CFRP strips-concrete Interface." *Industrial Construction*, 35(8), 31-35(in Chinese).

[7] Barros, J. A. O., Ferreira, D. R. S. M., Fortes, A. S. and Dias, S. J. E. (2006). "Assessing the effectiveness of embedding CFRP laminates in the near surface for structural strengthening." *Construction and Building Materials*, 20(7), 478-491.

[8] Teng, J. G., De Lorenzis, L., Wang, B., Li, R., Wong, T. N. and Lam, L. (2006). "Debonding failures of RC beams strengthened with near-surface mounted CFRP strips." *Journal of Composites for Construction, ASCE*, 10(2), 92-105.

[9] Lundqvist, J., Nordin, H., Täljsten, B. and Olofsson, T. (2005). "Numerical analysis of concrete beams strengthened with CFRP–A study of anchorage lengths." *Proceedings, International Symposium on Bond Behaviour of FRP in Structures (BBFS 2005)*, Hong Kong, China, 7-9 December, pp. 247-254.

[10] Lundqvist, J., Bernspång, L., Täljsten, B. and Olofsson, T. (2007). "A probability study of finite element analyses of near surface mounted carbon fiber reinforced polymer bonded to reinforced concrete." *Proceedings, 8th International Conference on Fibre Reinforced Plastics for Reinforced Concrete Structures*, Patras, Greece, 16-18 July, 2007 (CDROM).

[11] Sena Cruz, J. M., and Barros, J. A. O. (2004). "Modeling of bond between near-surface mounted CFRP laminate strips and concrete." *Computers and Structures*, 82(17-19), 1513-1521.

[12] Lu, X. Z., Ye, L. P., Teng, J. G. and Jiang, J. J. (2005). "Meso-scale finite element model for FRP sheets/plates bonded to concrete." *Engineering Structures*, 27(4), 564- 575.
[13] Chen, J.F. and Tao, Y. (2010). "Finite element modelling of FRP-to-concrete bond behaviour using the concrete damage plasticity theory combined with a plastic degradation model", *Proc. of the 5th International Conference on FRP Composites in Civil Engineering (CICE 2010)*, 27-29 Sept., Beijing, pp45-50.
[14] Li, X.Q., Chen, J.F. and Lu, Y. (2010). "Meso-scale modelling of FRP-to-concrete bond behaviour using LSDYNA". *Proceedings, 5th International Conference on FRP Composites in Civil Engineering (CICE 2010)*, Beijing, China, 27-29, September, pp. 494-498.
[15] Nanni, A., Bakis, C. E. and Boothby, T. E. (1995). "Test methods for FRP-concrete systems subjected to mechanical loads: State of the art review. " *Journal of Reinforced Plastics and Composites*, 14(6), 524-558.
[16] Yan, X., Miller, B., Nanni, A. and Bakis, C. E. (1999). "Characterization of CFRP bars used as near-surface mounted reinforcement." *Proceedings, 8th International Structural Faults and Repair Conference*, Edinburgh, UK (CD-ROM).
[17] CEB-FIP. (1990). *Model Code 90*, Lausanne, Switzerland, 1993.
[18] MSC.MARC (2005). User's Manual. *MSC. Software Corporation, 2 MacArthur Place, Santa Ana, California 92707, USA.*
[19] Teng, J. G., Zhu, W. C. and Tang, C. A. (2004). "Mesomechanical model for concrete—Part II: Applications." *Magazine of Concrete Research*, 56(6), 331-345.
[20] Zhu, W. C., Teng, J. G., and Tang, C. A. (2004). "Mesomechanical model for concrete—Part I: Model development." *Magazine of Concrete Research*, 56(6), 313-330.
[21] Yang, Z.J. and Chen, J.F. (2005). "Finite element modelling of multiple cohesive discrete crack propagation in reinforced concrete beams", *Engineering Fracture Mechanics*, 72(14), 2280-2297.
[22] Lu, X.Z., Jiang, J.J, Teng, J.G. and Ye, L.P. (2006). "Finite element simulation of debonding in FRP-to-concrete bonded joints", *Construction and Building Materials*, 20(6), 412-424.
[23] Rashid, Y. R. (1968). "Ultimate strength analysis of prestressed concrete pressure vessels." *Nuclear Engineering and Design*, 7, 334-344.
[24] Bazant, Z. P. and Oh, B. H. (1983). "Crack band theory for fracture of concrete." *Materials and Structures*, 16(93), 155-177.
[25] Buyukozturk, O. (1977). "Nonlinear analysis of reinforced concrete structures." *Computers and Structures*, 7, 149-156.
[26] Chen, W. F. (1982). *Plasticity in Reinforced Concrete*, New York: McGraw-Hill, 1982.
[27] Elwi, A. A. and Murray, D. W. (1979). "A 3D hypoelastic concrete constitutive relationship." *Journal of the Engineering Mechanics Division, ASCE*, 105(4), 623-641.
[28] Saenz, L. P. (1964). "Discussion of equation for the stress-strain curve of concrete, by Desayi and Krishnan." *Journal of the American Concrete Institute*, 61, 1229-1235.
[29] Hognestad, E. (1951). *A Study of Combined Bending and Axial Load in Reinforced Concrete Members*, University of Illinois Engineering Experiment Station, Bulletin Series No. 399.
[30] ACI-318 2008. *Building Code Requirements for Structural Concrete and Commentary*, ACI 318, Farmington Hills, MI.
[31] Hillerborg, A., Modeer, M. and Petersson, P. E. (1976). "Analysis of crack formation and crack growth in concrete by means of fracture mechanics and finite elements." *Cement and Concrete Research*, 6(6), 773-782.
[32] Petersson, P. E. (1981). *Crack Growth and Development of Fracture Zone in Plain Concrete and Similar Materials*, Report TVBM-1006, Division of Building Materials,

Lund Institute of Technology, Lund, Sweden.
[33] Hordijk, D. A. (1991). *Local Approach to Fatigue of Concrete*, PhD thesis, Delft University of Technology, 1991.
[34] Bazant, Z. P. and Gambarova, P. (1980). "Rough cracks in reinforced concrete." *Journal of the Structural Division, ASCE*, 106(4), 819-842.
[35] Walraven, J. C., and Reinhardt, H. W. (1981). "Theory and experiments on the mechanical behavior of cracks in plain and reinforced concrete subjected to shear loading." *Heron*, 26(1A), 1-68.
[36] Yamada, K. and Aoyagi, Y. (1983). "Shear transfer across crack." *Proceedings, JCI 2nd Colloquium on Shear Analysis of RC Structures*, October, 19-28.
[37] Okamura, H. and Maekawa, K. (1991). *Nonlinear Analysis and Constitutive Models of Reinforced Concrete*, Tokyo: Gihodo-Shuppan.
[38] Kang, Q. L. (1996). *Finite Element Analysis for Reinforced Concrete*, Beijing: China Water Power Press (in Chinese).
[39] Vecchio, F. J., and Lai, D. (2004). "Crack shear-slip in reinforced concrete elements." *Journal of Advanced Concrete Technology*, 2(3), 289-300.
[40] Rots, J. G. (1988). *Computational Modelling of Concrete Fracture*, PhD Thesis, Delft University of Technology, The Netherlands.
[41] Yu, T., Teng, J.G. and Chen, J.F. (2009). “Chapter 54: Mechanical properties of FRP composites”, in *ICE Manual of Construction Materials*, Thomas Telford Ltd., London, 641-647.
[42] Chen, J.F. and Pan W.K. (2006). “Three dimensional stress distribution in FRP-to-concrete bond test specimens”, *Construction and Building Materials*, 20(1-2), 46-58.
[43] Teng, J. G., Zhang, J. W., and Smith, S. T. (2002). "Interfacial stresses in reinforced concrete beams bonded with a soffit plate: A finite element study." *Construction and Building Materials*, 16(1), 1-14.

Table 1. Bond test specimen details

Specimen name	CS-30	CS-100	CS-150	CS-200	CS-250
Bond length (*mm*)	30	100	150	200	250
Groove width (*mm*)	9				
Groove depth (*mm*)	22				
CFRP strip thickness (*mm*)*	5				
CFRP strip width (*mm*)	16				
CFRP elastic modulus (G*Pa*)	120.8				
CFRP Poisson's ratio (G*Pa*)*	0.2				
Concrete compressive strength (*MPa*)	23.2				
Concrete tensile strength (*MPa*)	1.85				
Adhesive tensile strength (*MPa*)	42.6				
Adhesive elastic modulus (G*Pa*)	2.62				
Adhesive Poisson's ratio (G*Pa*)	0.35				
Ultimate load (*kN*)	14.82	36.28	46.07	54.47	64.02

*Assumed value

Table 2. Predicted ultimate loads and corresponding displacements for specimen CS-150

Shear retention model	Ultimate Load (kN)	Error	Corresponding displacement (mm)	Error
Test	46.1	NA	0.41	NA
Bazant and Gambarova's model [34]	50.3	9.1%	0.64	56%
Walraven and Reinhardt's model [35]	42.2	-8.5%	0.60	46%
Yamada and Aoyagi's model [36]	39.5	-14 %	0.45	9.8%
Okamura and Maekawa's model [37]	48.0	4.1%	0.43	4.9%
Kang's model [38]	42.3	-8.2%	0.37	-9.8%
Vecchio and Lai's model [39]	39.0	-15%	0.33	-20%

Table 3. Predicted and test ultimate loads for Li et al.'s tests [6]

Specimen Name	Test (kN)	FE Prediction (kN)	$\frac{\text{Prediction}}{\text{Test}}$
CS-30	14.8	17.7	1.20
CS-100	36.3	38.9	1.07
CS-150	46.1	48.0	1.04
CS-200	54.5	52.8	0.970
CS-250	64.0	59.8	0.934
Average =			1.04
STD =			0.100
COV =			0.0962

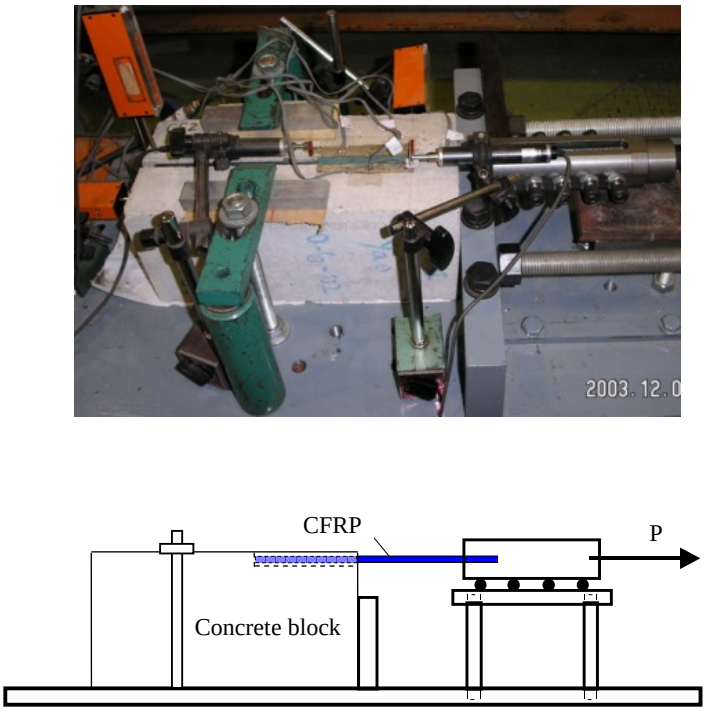

Fig. 1. Test setup of Li et al. [6]

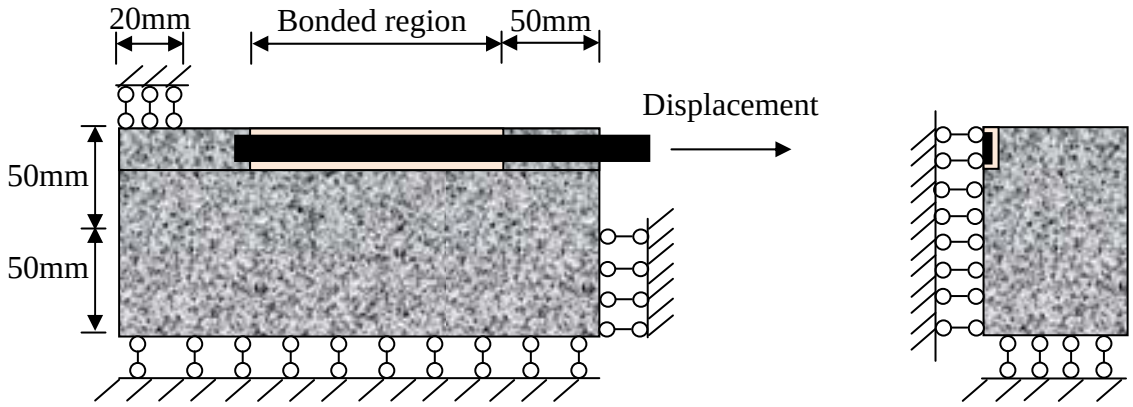

Fig. 2. Boundary conditions of the FE model

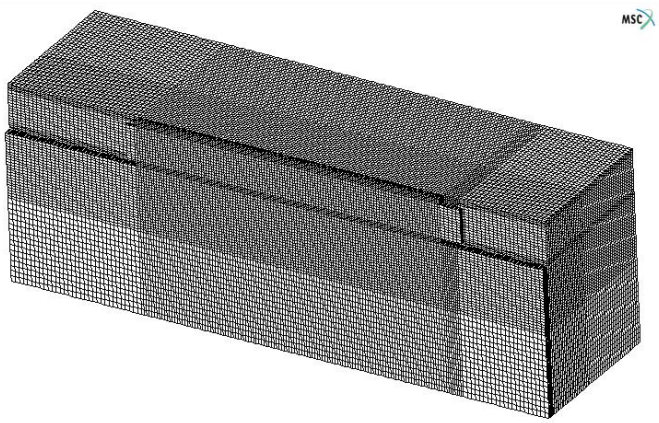

(a) Overall view

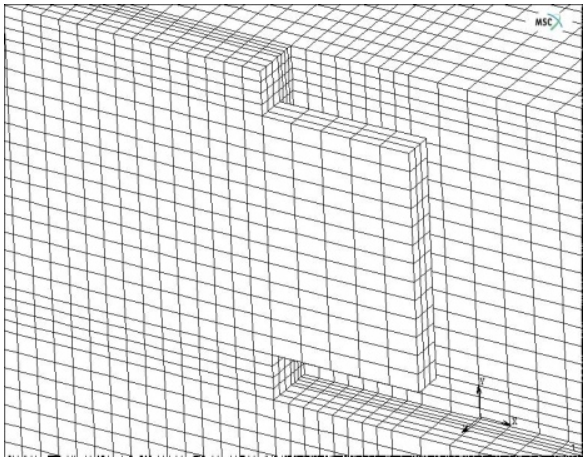

(b) Detailed view near the loaded end

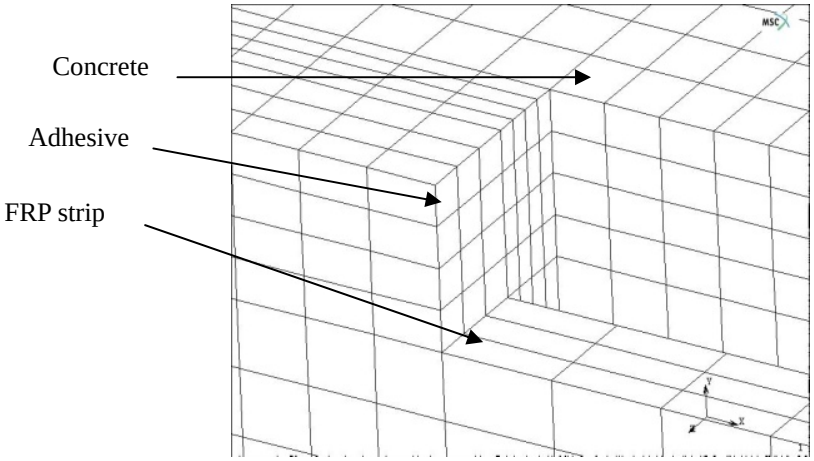

(c) Detailed view of the upper corner

Fig. 3. Mesh of specimen CS-150

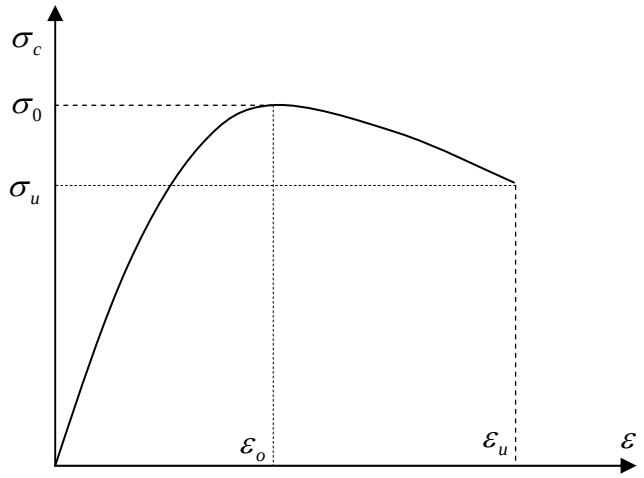

Fig. 4. Uniaxial compressive stress-strain curve for concrete

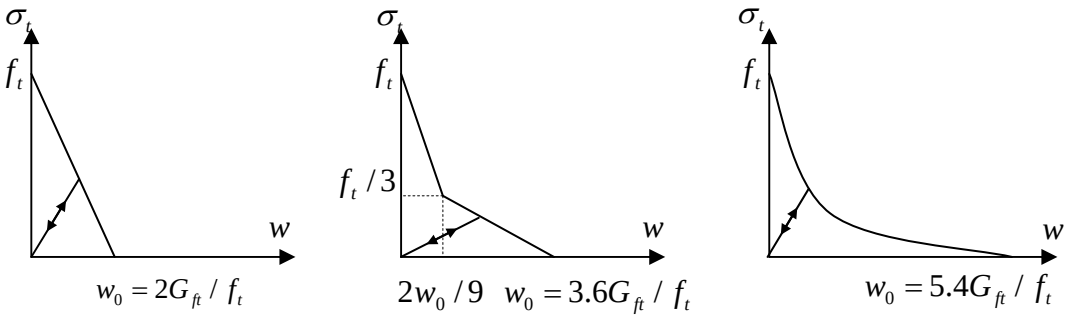

(a) Linear softening curve (b) Bilinear softening curve (c) Exponential softening curve

Fig. 5. Tension-softening curves

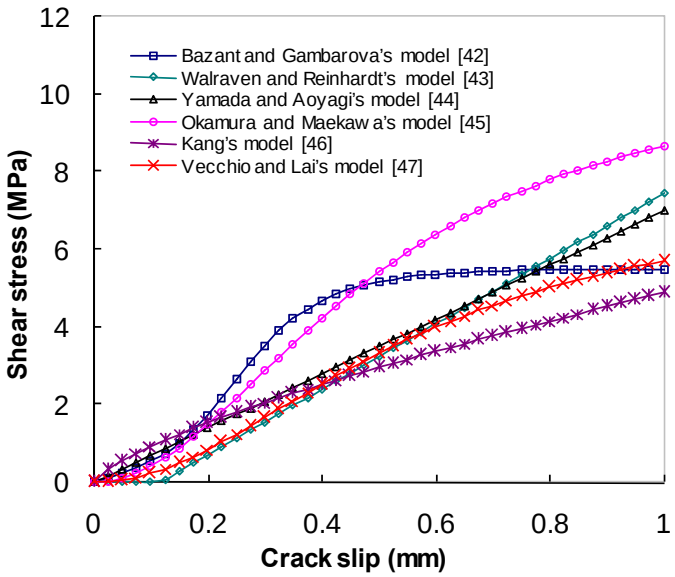

Fig. 6. Typical shear stress-slip curves of the six models studied (for crack width = 0.5mm)

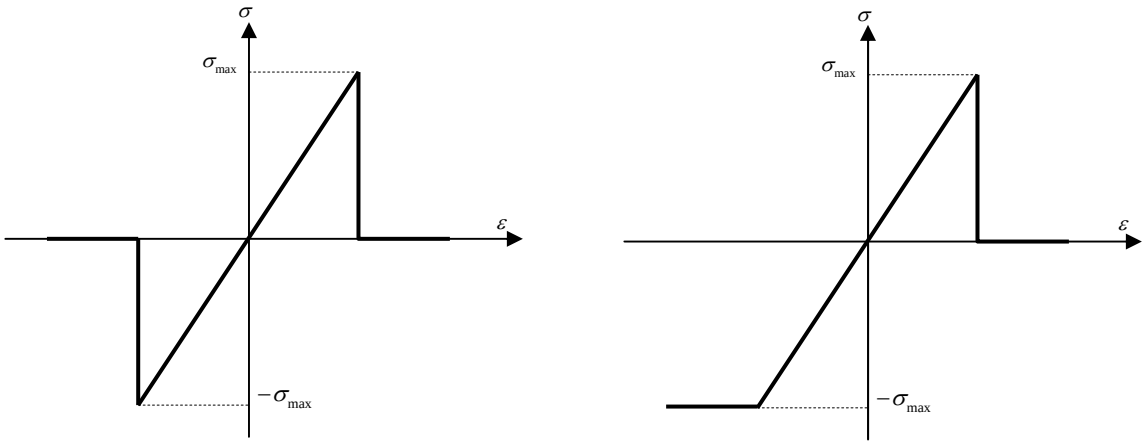

(a) FRP strip (b) adhesive

Fig. 7. Stress-strain curves for CFRP strip and adhesive

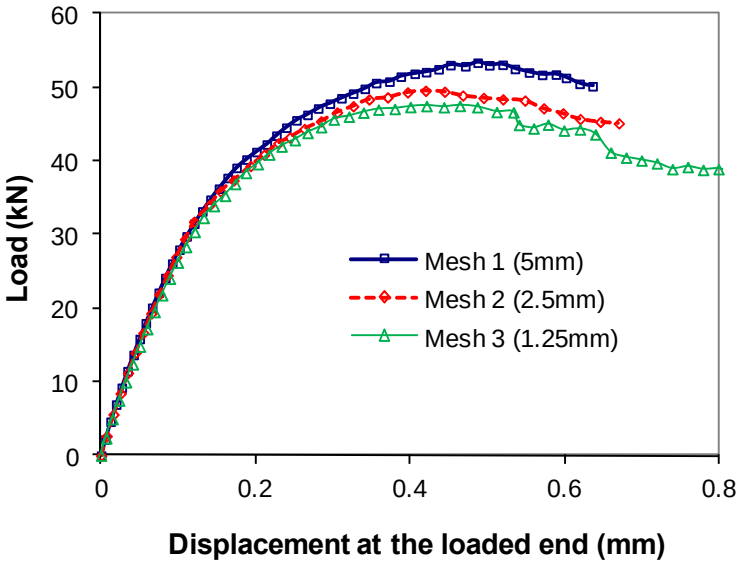

Fig. 8. Load-displacement curves obtained with three different FE meshes

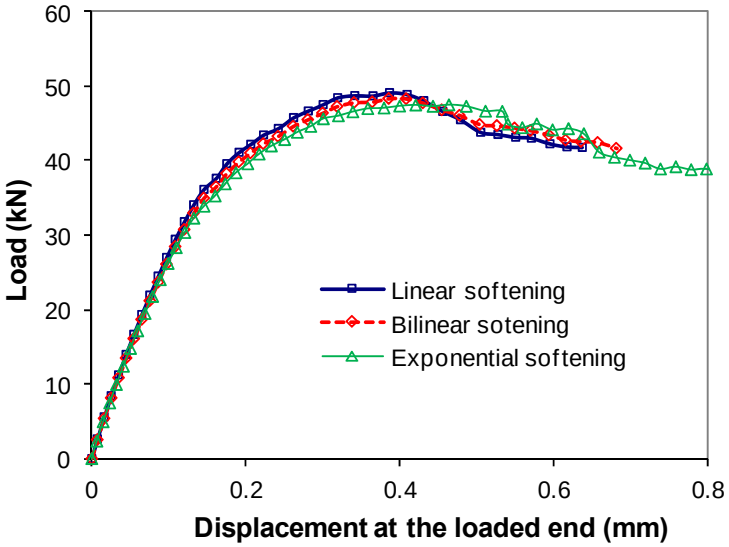

Fig. 9. Load-displacement curves obtained with three different tension-softening models

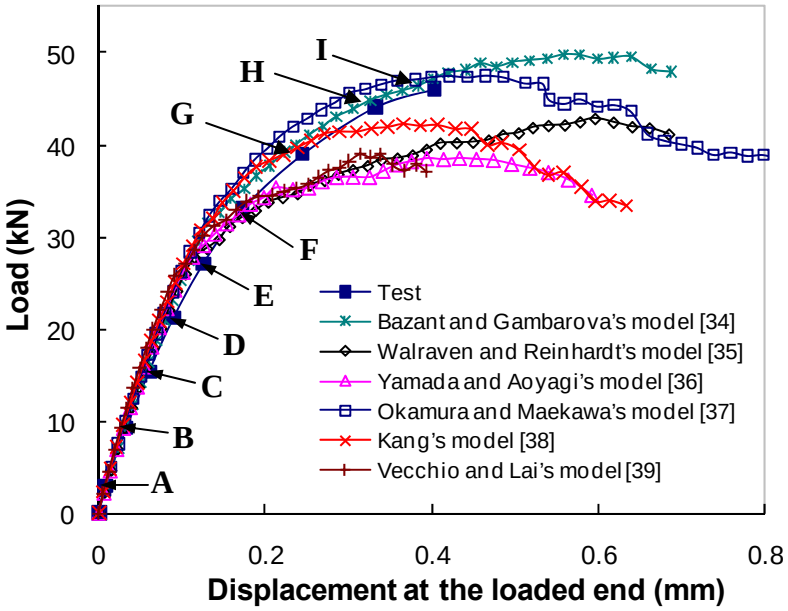

Fig. 10. Load-displacement curves obtained with six different shear retention models

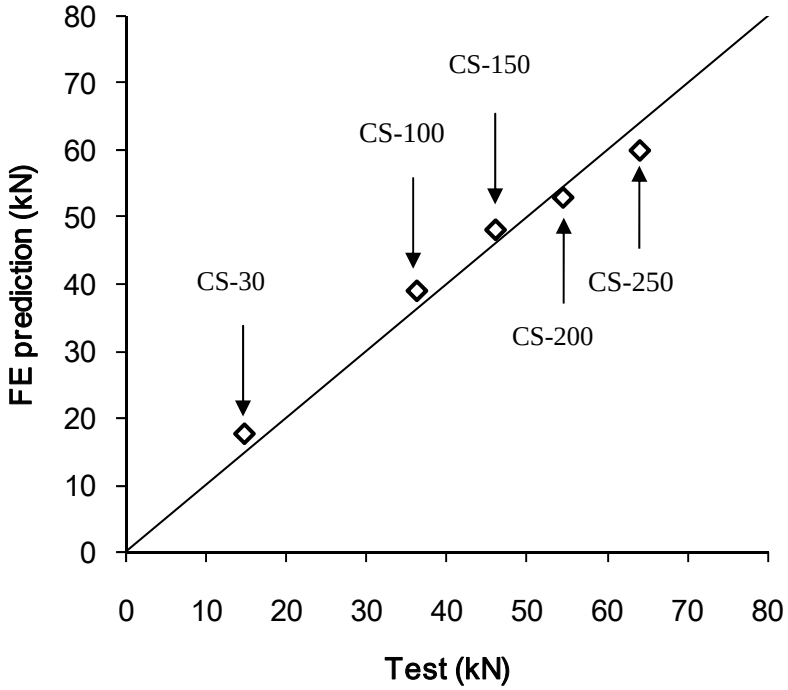

Fig. 11. Predicted ultimate load versus test ultimate load

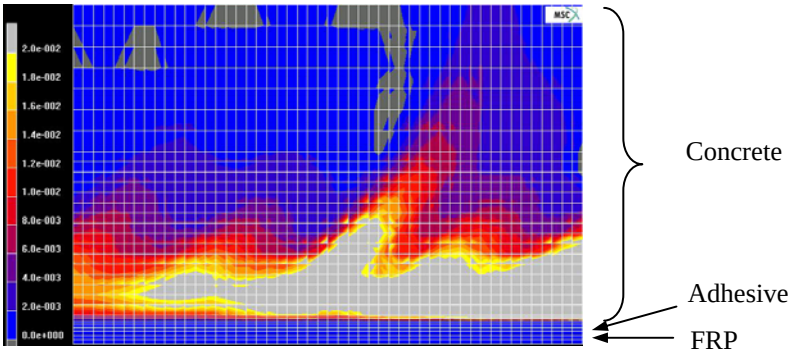

(a) Cracking strain pattern from the FE analysis

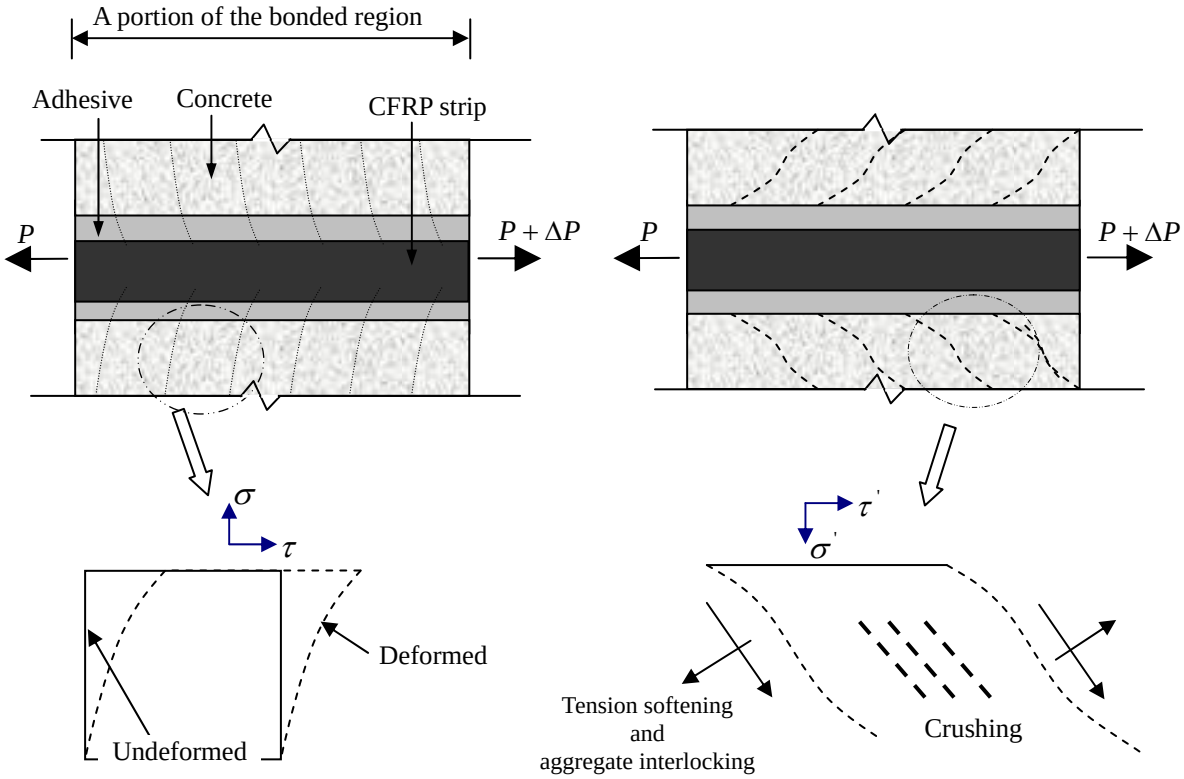

(b) Idealized pre-cracking deformation

(c) Idealized cracking pattern

Fig. 12. Deformation and cracking in concrete

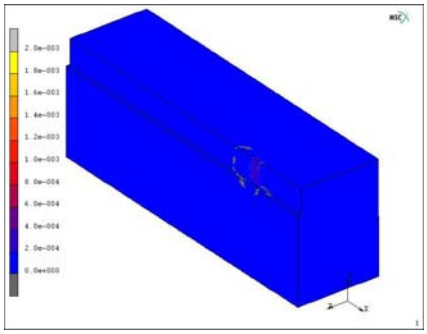

(a) P=0.06P_u (Point A)

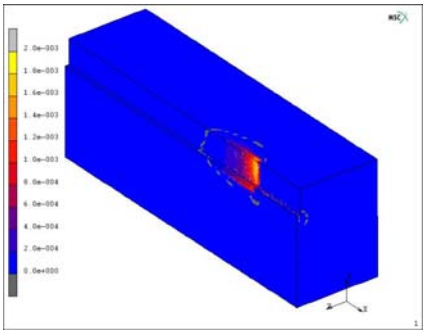

(b) P=0.20P_u (Point B)

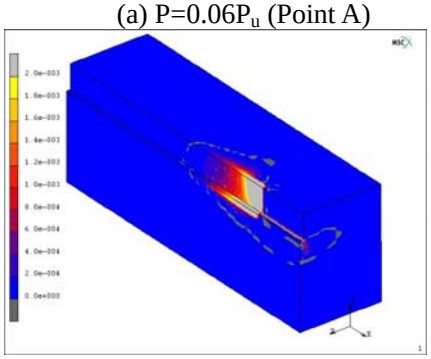

(c) P=0.33P_u (Point C)

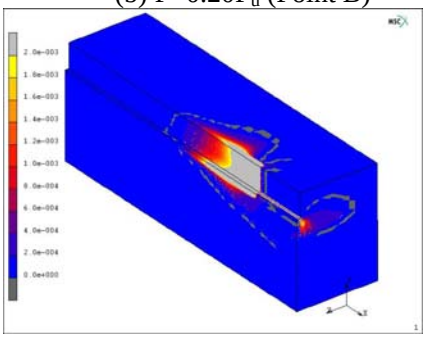

(d) P=0.46P_u (Point D)

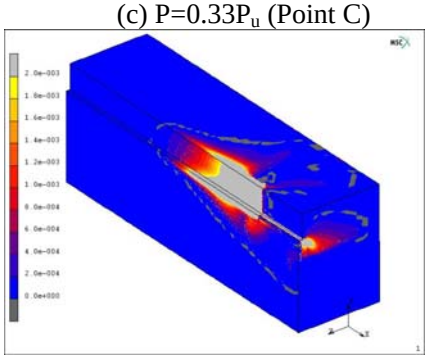

(e) P=0.59P_u (Point E)

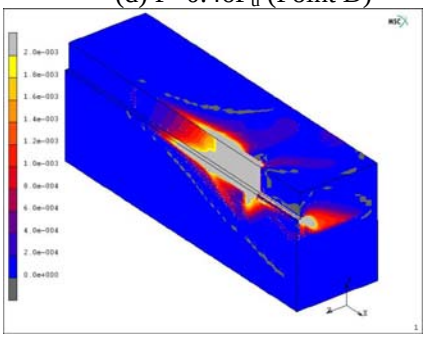

(f) P=0.72P_u (Point F)

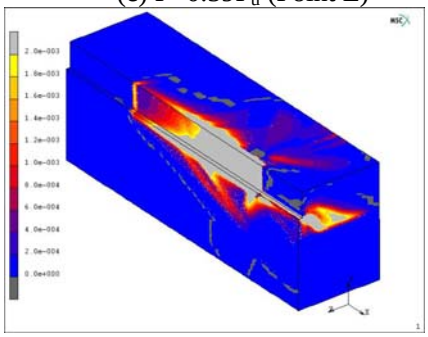

(g) P=0.85P_u (Point G)

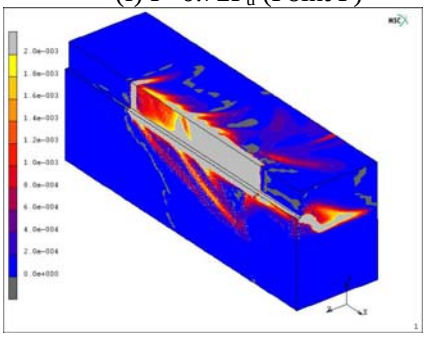

(h) P=0.96P_u (Point H)

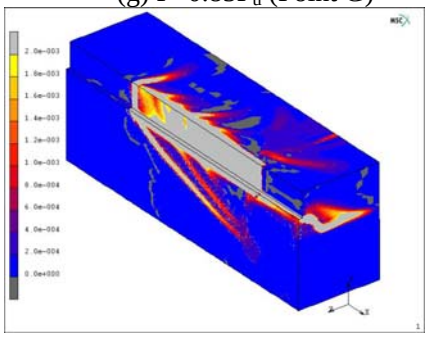

(i) P=P_u (Point I)

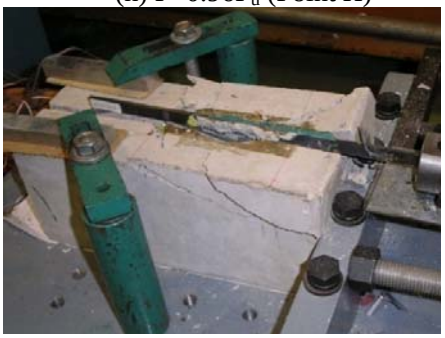

(j) Failure mode of the specimen

Fig. 13. Failure process of NSM CFRP strip-to-concrete bonded joint

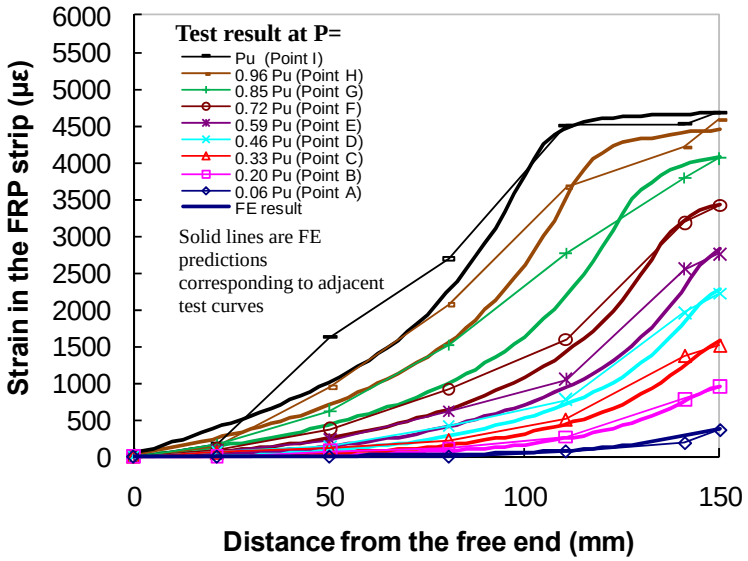

Fig. 14. Comparison of strain distributions in the FRP between test and FE analysis (Note: The strain distributions from FE analysis were adjusted for clearer comparisons in accordance with the ultimate load ratio between test and FE analysis, which is 0.96)

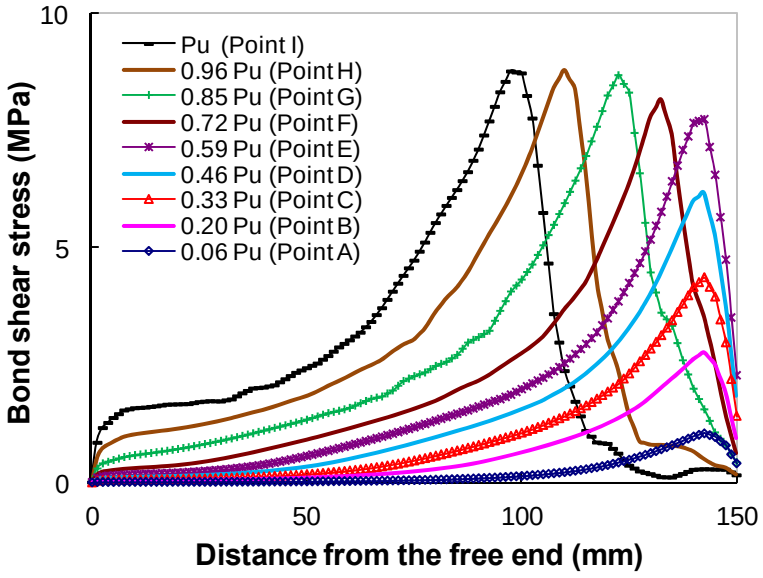

Fig. 15. Bond shear stress distributions from FE analysis

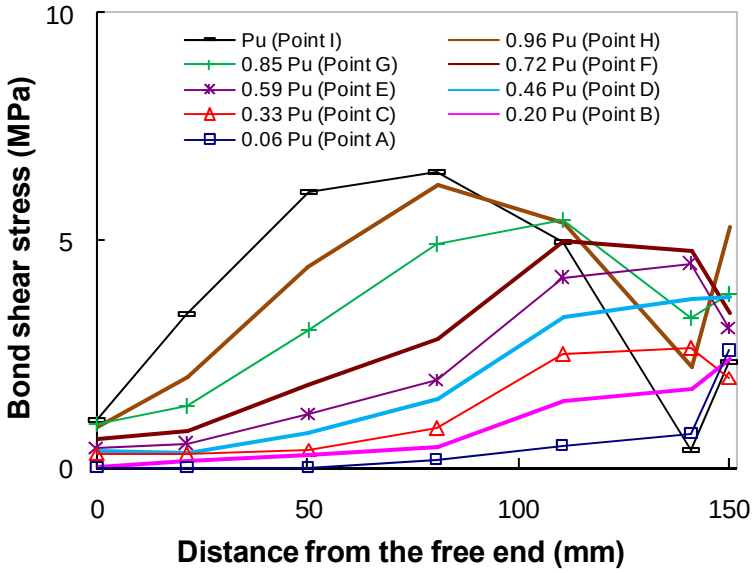

Fig. 16. Bond shear stress distributions deduced from strain measurements

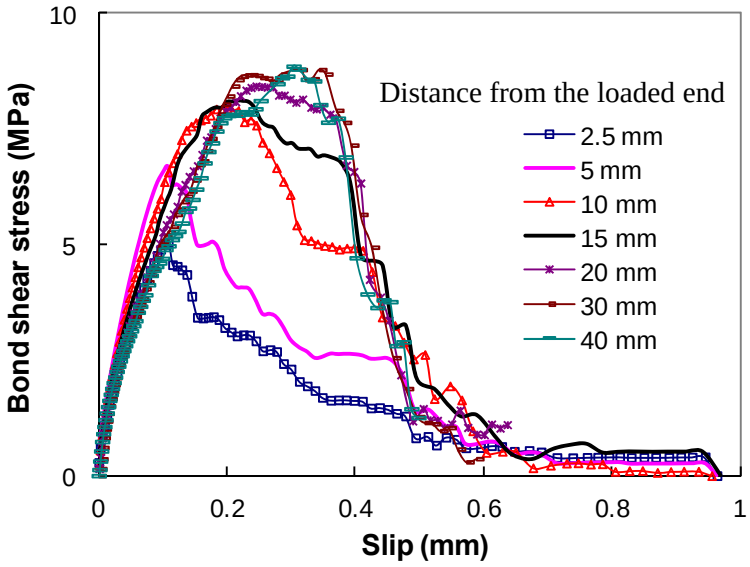

Fig. 17. Local bond-slip curves from FE analysis